SAR Image Segmentation with Structure Tensor Based Hierarchical Student's t-Mixture Model

Huilin Ge[1], Yahui Sun[2], Yueh-Min Huang[3], Se-Jung Lim[4]

[1] School of Electronics and Information, Jiangsu University of Science and Technology, China
[2] School of Computer and Software, Nanjing University of Information Science and Technology, China
[3] Department of Engineering Science and Institute of Education, National Cheng-Kung University, Taiwan
[4] Liberal Arts & Convergence Studies, Honam University, Republic of Korea
ghl1989@just.edu.cn, sun_yahui105@126.com, huang@mail.ncku.edu.tw, limsejung@korea.ac.kr

Abstract

Synthetic aperture radar (SAR) plays an important role in Satellite IoT, due to its remarkable capability of all-weather monitoring and information acquisition under complicated conditions. It is well-known that SAR image interpretation usually requires accurate segmentation. However, SAR image segmentation inevitably encounters speckle noise because of the unique imaging mechanism of SAR. In order to address the problem, we proposed SAR images segmentation method by combined a hierarchical Student's t-mixture model (HSMM) with an anisotropic mean template, which can divide the global SAR image segmentation into several sub-clustering-issues efficiently resolved using classical algorithm. With the aid of a non-linear structure tensor for image contents analysis, the adaptive template can explore more spatial correlations between pixels for the purpose of improving HSMM robustness and segmentation accuracy. Experiments results both synthetic and real SAR images demonstrate that our proposed HSMM is more robust to speckle noise and obtains more accurate segmented images.

Keywords: Sensor data processing, Machine learning, SAR image segmentation, Satellite IoT

1 Introduction

With the rapid development of IoT techniques and space exploration techniques, the satellite IoT as a new and high technique has drawn more attention from the whole world, for the reason that it can achieve global coverage for observing inaccessible areas and its sensor layout is hardly limited by space. In order to implement all-weather monitoring and intelligent abnormal perception, the satellite IoT has various imaging instruments. Among them, the synthetic aperture radar is a valuable imaging load, due to its capability of acquisition under complicated conditions [1-2].

Segmentation is a task of dividing an image into different homogeneous areas [3]. In each consistent region, the pixels share similar attributes and obey the same statistical distribution [4-6]. In SAR image processing and analysis chain, segmentation plays a very important role for subsequent stages such as interpretation and understanding. However, because of its unique imaging principles, SAR image inevitably suffers from speckle noise, which can be viewed as multiplicative noise and usually results in the inhomogeneity problem of image intensities. Compared with natural image [7], segmentation is more challenging for SAR image [8].

In the past decades, variousimage segmentation methods for SAR-image have been proposed [9-12], which can be roughly divided into four categories: the level set based [13-15], the super-pixel based [16-18], the graphical model based [19-21], and the clustering based [22-25]. The level set method utilizes Hamilton-Jacobi model and generates segmented results with binary values. This method can be viewed as a fast implementation of active contour model. Superpixels usually denote to a cluster of locally adjacent pixels with homogenous feature, resulting from over-segmentation technique. Compared with the pixel based method, the super-pixel-based approach is robust to outliers. The graphical model-based method considers image as a graph, where its node represents pixel and edge stands for the relationship of pixels. Based on the structure, image segmentation is implemented through minimizing a energy function with optimization technique as graph-cut. Clustering method classifies the objects in the feature space according to a certain similarity criterion, with the aim at ensuring that similar pixels belong to the same class. the clustering-based image segmentation methods have made rapid progress in recent few years. Based on the observation, this work focuses the finite mixture model (FMM) based segmentation approach [26-28].

*Corresponding Author: Se-Jung Lim; E-mail: limsejung@korea.ac.kr
DOI: 10.3966/160792642020052103001

FMMs have proven to be successful for data clustering, which assume that the heterogeneous data can be represented by a mixture of a finite number of probability statistics functions with same type distribution but different parameters [29]. When the distribution function is selected as Gaussian distribution, the FMM called Gaussian mixture model (GMM). One can employ GMM to model observed data with weighted components, where the weight reveals the contribution of a gaussian components and is estimated by using expectation maximization (EM) algorithm along with mean and covariance matrix. Although Gaussian distributions computation is easy to explement and the related GMM its variations is efficient to model data and widely investigated for image clustering, they often encounter robustness problem, that is sensitive to outliers. Recently, the Student's t-distribution has received more and more attention in machine vision applications such as image recovery, image segmentation, feature selection and image classification [30-32]. Because of the heavy tail of the Student's t-distribution, it can be used as component to improve the robustness of FMM to noise and other interferences, which gives rise to the Student's t-mixture model (SMM). Compared to GMM, SMMs can obtain more better performance on data modelling and representation. However, few of them take into account the spatial correlations among neighborhood pixels, therefore influencing their further applications.

For handling the above-mentioned problem in FMMs recently, Markov random field (MRF) [33-35] technique has been combined with the FMMs [36-40], which attempt to introduce spatially local dependent information into the segmentation process of FMMs. For instance, [34] early introduced a spatially constrained FMM, which describes the pixel label as a random variable and assumes that the label variable conforms to the Markov prior field. In the work, the maximum posterior probability estimation (MAP) and the EM algorithm are used as the model parameter optimization method. This method enhances the spatial smoothness of the pixel label and enables segmentation spatially continuous. Later, a spatially variant FMM (SVFMM) based image segmentation algorithm was presented by Blekas [40] to improve the computation of pixel label values through quadratic programming. Recently, a new approach with the hidden Markov random model (HMRF) was proposed by Zhang [35] for image segmentation. However, the state of HMRF is not observable directly and needs to estimation and calculation. Moreover, HMRF based image segmentation methods are time consuming and difficult to implement [41]. In addition, an extra parameter requires to estimate for tuning the image smoothing extent. In fact, the optimal value of the parameter is difficult to determine. It should be set sufficiently large to tolerate the noise in image. However, if one attempts to preserve image details and textured contents, the value of the tuning parameter must be set small enough. Obviously, the two conditions are hard to fulfil, simultaneously. It should be note that the aforementioned image segmentation methods using FMM and MRF frequently utilized Gaussian distribution, hence leading to limited performance. To handle the issue, a SAR image segmentation approach with SMM called MSMM was presented by Zhang et al [25], which employed a mean template to explore spatial local correlation and introduced it into SMM. Based on the work of [25], a modified version of MSMM was suggested in [42], which followed the idea of hierarchical mixture of experts scheme [37] and replaced the SMM with a hierarchical Student's mixture model (HSMM). The variant method can enhance segmentation performance of MSMM. However, the mean template fails to be adaptive to image contents and the behavior of SMM jointed with it is isotropic.

Based the above-mentioned observation, a weighted mean template is introduced in this work, which used linear structure tensor [43-44] to analyze and estimate image contents with the aim at improving the performance of MSMMs on SAR images. The structure tensor is popular used in computer vision filed to analyze image structures. In this work, a non-linear structure tensor to construct new weighted mean template to make it more better adaptive to image structures. In other words, the template is content-aware and therefore truly geometric and improve the segmentation accuracy of MSMM method in SAR images. Our proposed method decomposes the clustering problem into two levels to solve. We break up the clustering problem into smaller sub-problems, and then deal with these sub-problems. Then, we utilize the EM algorithm for parameters optimization, considering its simplicity and stability. Moreover, more experiments are conducted to evaluate the herein proposed segmentation approach.

The rest of this paper is organized as follows. In Section 2, we shortly introduce the Student's t-distribution and the FMM, respectively. A new weighted mean template using adaptive structure tensor is presented in Section 3. Section 4 describes our proposed SAR image segmentation method, i.e., HSMM in details. Segmentation experimental results are shown in Section 6. Finally, we conclude our work in Section 7.

2 Preliminaries

2.1 Student's t-Distribution

Generally, one-dimensional Student's t-distribution can be obtained as follows: take out the conjugate transcendental of the accuracy of one-dimensional Gaussian distribution, and then integrate the precision variables. Thus, it can be linearly represented by

multiple Gaussian distribution functions with the same mean parameter but different variance parameters, written as follows:

$$S(x \mid \mu, \varepsilon, \tau) = \frac{\Gamma(\frac{\pi}{2}+\frac{1}{2})}{\Gamma(\frac{\pi}{2})}(\frac{\varepsilon}{\pi\tau})[1+\frac{\varepsilon(x-\tau)^2}{\tau}]^{-(\frac{\tau-1}{2})} \quad \textbf{(1)}$$

where x is a one-dimensional observed variable, μ denotes the mean parameter of Gaussian distribution, ε refers to the precision, and τ stands for the freedom degree. Especially, when $\tau = 1$, the Student's t-distribution can be viewed as the Cauchy-distribution. In equation (1), $\Gamma(\bullet)$ is the gamma function written as

$$\Gamma(v) = \int_0^{\infty} t^{v-1} e^{-t} dt \quad \textbf{(2)}$$

For multivariate observed data $y \in R^L$, its probability density function (PDF) of Student's t-distribution can be defined by multivariate Gaussian distribution function with the Wishart prior as

$$S(y \mid \mu, \Sigma, \tau) = \frac{\Gamma(\frac{\pi}{2}+\frac{1}{2})}{\Gamma(\frac{\pi}{2})} \frac{|\Sigma|^{\frac{1}{2}}}{(\pi\tau)^{\frac{L}{2}}} \times [1+\frac{(y-\mu)^T \Sigma (y-\mu)}{\tau}]^{-(\frac{\tau}{2}+\frac{L}{2})} \quad \textbf{(3)}$$

In (3), when τ is to be $\tau \to \infty$, Student's t-distribution degenerates to a Gaussian distribution. As known that the Student's t-distribution offers a form of generalization of the Gaussian distribution and has heavy tail which enable its maximum likelihood parameters more robust to outliers. Moreover, compared with GMM, SMM can improve performance of FMM on model parameter estimation, and achieve better computational efficiency and stability [39].

2.2 FMM

FMMs are mixtures of density functions to describe observed data, which is a linear superposition of multiple distribution function with the same family of distribution but different parameters. Let $J = \{k\}_{j=1}^{K}$ be the class labels of an image, $D = \{d\}_{d=1}^{M}$ stands for image intensity value range, and $X = \{x_i : (x_i \in Q \; and \; i \in N)\}$ denotes the Label set of image Y. Denote $Y = \{y_i\}_{i=1}^{N}$ be a SAR image with size of N, which can be partitioned intro K clusters. y_i refers to the observed value at pixel i and x_i is the related class label. The probability that x_i belongs to class j can be written as:

$$p(x_i = i) = \pi_j \quad \textbf{(4)}$$

where π_j stands for the prior probability of pixel i which satisfies the constrains:

$$0 \le \pi_j \le 1 \text{ and } \sum_{j=1}^{K} \pi_j = 1 \quad \textbf{(5)}$$

Denote Θ the set of model parameter in FMM, that is $\Theta = \{\pi_j ; \theta_j \mid j \in Q\}$. The joint distribution of class label and image pixel is calculated as follows:

$$\begin{aligned} p(x, y \mid \Theta) &= \prod_{j=1}^{K} p(x_i, y_i \mid \Theta) \\ &= \prod_{j=1}^{K} p(y_i \mid x_i, \Theta) p(x_i, \Theta) \\ &= \prod_{j=1}^{K} (\pi_{x_i} p(y_i \mid \theta_j)) \end{aligned} \quad \textbf{(6)}$$

when $Y_i = y_i$, the marginal distribution function can be defined by:

$$\begin{aligned} p(y_i \mid \Theta) &= \sum_{j=1}^{K} p(X_i = j, y_i \mid \Theta) \\ &= \sum_{j=1}^{K} p(y_i \mid X_i = j, \theta_q) p(X_i = j) \\ &= \sum_{j=1}^{K} \pi_j p(y_i \mid \theta_j) \end{aligned} \quad \textbf{(7)}$$

FMM has drawn much attention in estimation of data distributions and clustering analysis owing to its capability of approximating and modelling complex distributions. However classical FMM merely applies histogram classification scheme for image segmentation, which often suffers from the problem of error segmentation. In practice, images with same histogram contain totally different contents in many cases. Therefore, more content-aware related information requires to be explored and introduced into FMM to enhance its performance.

3 Adaptive Structure Tensor Based Mean Template

In this work, a novel mean template is proposed and introduced into SMM, which utilizes the adaptive nonlinear structure tensor to estimate image contents in the neighborhood of current pixel and therefore can enhance the capability of mean template in exploring correlations between pixels. With our mean template, (7) can be rewritten as follows:

$$p(y_i \mid \Theta) = \sum_{j=1}^{K} \pi_j \prod_{q \in \Lambda_i} p(y_i \mid \theta_j)^{\frac{w_q}{R_i}} \quad \textbf{(8)}$$

where Λ_i stands for the set of pixels among the neighborhood center around pixel *i*, and r_i denotes the normalization factor calculated by

$$R_i = \sum_{q \in \Lambda_i} w_q \tag{9}$$

where w_q refers to the weight coefficient, which can be computed using the Euclidean distance [42], that is $w_q = \frac{1}{1+L_{qi}^2}$, where L_{qi} is for the Euclidean distance between the i^{th} and q^{th} pixels. It is worth noting that the Euclidean distance only computes the distance information among pixels, which is hard to describe pixel similarity. In fact, image similarity computation often plays an important role in regularization. In the herein proposed paper, we employ structure tensor to represent and calculate w_m as follows:

$$\begin{cases} w_q = \dfrac{1}{1+E_{q_i}^2} \\ E_{qi} = |\, tr(S_q) - tr(S_i)\,| \\ S_i = g_p * (\nabla Y_i \nabla Y_i^T) = g_p * \begin{pmatrix} Y_1Y_1 & Y_1Y_2 \\ Y_1Y_2 & Y_2Y_2 \end{pmatrix}_i \end{cases} \tag{10}$$

where E_{qi} is a local energy measure (LEM) defined by the difference of the traces of matrices S_q and S_i, S_i is the linear structure tensor calculated through convolving $\begin{pmatrix} Y_1Y_1 & Y_1Y_2 \\ Y_1Y_2 & Y_2Y_2 \end{pmatrix}$ using Gaussian filter g_ρ with smoothing scale ρ, and $\nabla Y_1 = (Y_1, Y_2)^T$ is the image gradient.

Structure tensor, a smoothed second-moment matrix of image, has been shown to be a useful tool for image analysis in computer vision. Its eigenvectors and eigenvalues are usually been employed and exploited to discriminate image edges, corners and flat regions. In this paper, we utilize it to describe image similarity between the current pixel *i* and pixel *q* among the neighborhood of the current pixel *i*.

Here define the two eigenvalues of structure tensor *S*, as λ_1 and λ_2, the two corresponding orthogonal eigenvectors as γ_1 and γ_2. Then, they can be calculated by:

$$\lambda_{1,2} = \frac{1}{2}(s_1 + s_3 \pm \sqrt{(s_1 - s_3) + 4(s_2)^2}),\ \lambda_1 \geq \lambda_2 \tag{11}$$

$$\gamma_2 = \begin{bmatrix} s_3 - s_1 + \sqrt{(s_1 - s_3)^2 + 4(s_2)^2} \\ -2s_2 \end{bmatrix} \tag{12}$$

$$\gamma_2 = \begin{bmatrix} s_3 - s_1 + \sqrt{(s_1 - s_3)^2 + 4(s_2)^2} \\ -2s_2 \end{bmatrix} \tag{13}$$

where s_1, s_2 and s_3 denotes Y_1Y_1, Y_1Y_2 and Y_2Y_2, respectively. Based on the two eigenvalues and eigenvectors, structure tensor *S* can be rewritten as:

$$S = \lambda_1\gamma_1\gamma_1^T + \lambda_2\gamma_2\gamma_2^T \tag{14}$$

With structure tensor *S*, one can use its eigenvalues to detect image local contents such as flat regions, corners, textures and edges. In addition, the eigenvectors are often employed to represent the direction of image structure.

Classical SMM based clustering methods assume that pixels in image are independent to each other, which still fails to achieve satisfying results. To address the problem, the mean template technique was introduced into SMM to explore more information in neighbourhood of current pixel. Although the SMM with mean template can enhance the perform of SMMs, the mean template is linear. In other word, this technique tests each pixel in the same manner, which is not adaptive. Our proposed template is content-aware, where the weighting coefficients are adaptive to image structures due to analysis of structure tensor to image contents.

4 Proposed HSMM Based SAR Image Segmentation

In this section, we introduce a novel hierarchical Student's t-mixture model (HSMM) for SAR image segmentation. First, to incorporate more image content information, the prior probability π_j can be modified as π_{ij}, then the conditional probability (8) is rewritten as

$$p(y_i \mid \Theta) = \sum_{j=1}^{K} \pi_{ij} \prod_{q \in \Lambda_i} p(y_i \mid \theta_j)^{\frac{w_q}{R_i}} \tag{15}$$

where π_{ij} is prior with the constraint conditions as follows:

$$0 \leq \pi_j \leq 1 \text{ and } \sum_{j=1}^{K} \pi_{ij} = 1 \tag{16}$$

It is well-known that image segmentation with traditional FMM is a statistics method based on an image histogram. The aforementioned models including the GMM, the SMM and theirs variations view the histogram as to be isotropic. In other words, the shape of image histogram is usually assumed to be symmetric. However, in practical applications, with the advent of high-resolution imaging devices, for many acquired images, their histograms are not symmetric.

To handle this issue, we introduce a novel SMM with the aim of accurately representing the image histogram with non-symmetric shape of distribution. Our proposed HSMM can be defined by:

$$p(y_i \mid \pi, k, \theta) = \sum_{j=1}^{K} \pi_{ij} \sum_{m=1}^{M} k_{ijm} \prod_{q \in \Lambda_i} S(y_i \mid \theta_{jk})^{\frac{w_q}{R_i}} \quad (17)$$

where $S(y_i \mid \theta_{jk})$ is defined with equation (3). Its full form is given in (18):

$$\begin{aligned} S(y_i \mid \mu_{jm}, \Sigma_{jm}, \tau_{jm}) &= \frac{\Gamma(\frac{v_{jm}}{2} + \frac{L}{2})}{\Gamma(\frac{v_{jm}}{2})} \frac{|\Sigma_{jm}|^{\frac{1}{2}}}{(\tau_{jm}\pi)^{\frac{L}{2}}} \\ &\times [1 + \frac{(y_i - \mu_{jm})^T \Sigma (y_i - \mu_{jm})}{\tau_{jm}}]^{-(\frac{\tau_{jm}}{2} + \frac{L}{2})} \end{aligned} \quad (18)$$

The model parameter $\theta_{jm} = \{\mu_{jm}, \Sigma_{jm}, v_{jm}\}$. In (17), k_{ijm} is a sub-prior probability with the following constraints as:

$$k_{ijm} \geq 0 \text{ and } \sum_{m=1}^{M} k_{ijm} = 1 \quad (19)$$

With Eq. (17), the likelihood function of SAR image with *N* pixels is defined as follows:

$$p(Y \mid \pi, k, \theta) = \prod_{i=1}^{N} \sum_{j=1}^{K} \pi_{ij} \sum_{m=1}^{M} k_{ijm} \prod_{q \in \Lambda_i} S(y_i \mid \theta_{jm})^{\frac{w_q}{R_i}} \quad (20)$$

The logarithmic likelihood function is obtained by taking a natural logarithm of (20):

$$\begin{aligned} L &= \log p(Y \mid \pi, m, \theta) \\ &= \sum_{i=1}^{N} \log \left[\sum_{j=1}^{K} \pi_{ij} \sum_{m=1}^{M} k_{ijm} \right] \prod_{q \in \Lambda_i} S(y_i \mid \theta_{jm})^{\frac{w_q}{R_i}} \end{aligned} \quad (21)$$

According to [23], we optimize the complete data function (21) through setting the model parameters $\Phi = \{\pi_{ij}, k_{ijm}, \eta_{ij}, z_{ijm}, \mu_{jm}, \Sigma_{jm}, \tau_{jm}\}$, hence achieving an objective function given in (22).

An advantage of the proposed method is the establishment of (17) which jointly consider the pixel intensity values and image content information. Another improvement is that we introduce a weight mean template into the conditional probability to try to utilize more image prior knowledge during neighborhood pixels. The contributions we proposed are summarized as follows:

1. Introduce a hierarchical FMM for image segmentation to enhance the standard FMM robustness to the noise.
2. Utilize the multivariate Student's t-distribution to calculate the conditional probability.
3. Consider the effect of the spatial information on the image pixels.
4. Incorporate a weight mean template into the conditional probability.

5 Parameters Estimation

In this section, we introduce the parameter estimation method through utilizing EM algorithm to solve Eq. (22).

$$\begin{aligned} J(\Phi) &= \sum_{i=1}^{N} \sum_{j=1}^{K} \eta_{ij} E_{\Phi} \left\{ \log \pi_{ij} + \log \left[\sum_{m=1}^{M} k_{ijm} \prod_{q \in \Lambda_i} S(y_i \mid \theta_{jm})^{\frac{w_q}{R_i}} \right] \right\} \\ &= \sum_{i=1}^{N} \sum_{j=1}^{K} \eta_{ij} \left\{ \log \pi_{ij} + \sum_{m=1}^{M} z_{ijm} E_{\Phi} \right. \\ &\quad \left. \left[\log k_{ijm} + \log \prod_{q \in \Lambda_i} S(y_i \mid \theta_{jm})^{\frac{w_q}{R_i}} \right] \right\} \\ &= \sum_{i=1}^{N} \sum_{j=1}^{K} \eta_{ij} \left\{ \log \pi_{ij} + \sum_{m=1}^{M} z_{ijm} \right. \\ &\quad \left. \left[\log k_{ijm} + E_{\Phi} \left(\sum_{q \in \Lambda_i} \frac{w_q}{R_i} \log S(y_i \mid \theta_{jm}) \right) \right] \right] \end{aligned} \quad (22)$$

In E-step, we respectively calculate the posterior probability and sun-posterior probability as follows:

$$\eta_{ij} = \frac{\pi_{ij} p(y_i \mid \pi, k, \theta)}{\sum_{h=1}^{K} \pi_{ih} p(y_i \mid \pi, k, \theta)} \quad (23)$$

$$z_{ijm} = \frac{k_{ijm} S(y_i \mid \mu_{jm}, \Sigma_{jm}, \tau_{jm})}{\sum_{n=1}^{M_j} k_{ijm} S(y_i \mid \mu_{jn}, \Sigma_{jn}, \tau_{jn})} \quad (24)$$

To exploit image content information in the neighborhood pixels, the proposed mean template combined with adaptive structure tensor is introduced into the probabilities of posterior and sub-posterior, respectively. Thus, the probabilities in (23) and (24) can be modified as

$$\eta_{ij} = \frac{\pi_{ij} \prod_{q \in \Lambda_i} p(y_i \mid \pi, k, \theta)^{\frac{w_q}{R_i}}}{\sum_{h=1}^{K} \pi_{ih} \prod_{q \in \Lambda_i} p(y_i \mid \pi, k, \theta)^{\frac{w_q}{R_i}}} \quad (25)$$

$$z_{ijm} = \frac{k_{ijk} \prod_{q \in \Lambda_i} S(y_i \mid \mu_{jk}, \Sigma_{jk}, v_{jk})^{\frac{w_q}{R_i}}}{\sum_{n}^{M_j} k_{ijn} \prod_{q \in \Lambda_i} S(y_i \mid \mu_{jn}, \Sigma_{jn}, v_{jn})^{\frac{w_q}{R_i}}} \quad (26)$$

A Student's t-distribution $S(\mu_{jm}, \Sigma_{jm}, v_{jm})$ is used for the conditional probability in the HSMM. Actually, the Student's t-distribution can be viewed as a Gaussian distribution $g(\mu_{jm}, \Sigma_{jm}, u_{ijm})$ with an accurate scale factor u which obeys the following distribution as

$$u_{ijm} = \frac{\tau_{jm} + L}{\tau_{jm} + (y_i - \mu_{jm})^T \sum_{jm}^{-1} (y_i - \mu_{jm})} \tag{27}$$

Then, in M-step, the prior π_{ij} is estimated at first. Using the Lagrange multiplier λ_i, the derivative of the prior probability π_{ij} for each data point can be written as

$$\frac{\partial}{\partial \pi_{ij}} \left[J(\Theta) - \sum_{i=1}^{N} \lambda_i \left(\sum_{j=1}^{M} \pi_{ij} - 1 \right) \right] = 0 \tag{28}$$

Using (22), (28) can be written

$$\eta_{ij} \frac{1}{\pi_{ij}} - \lambda_i = 0 \tag{29}$$

Under the constrains (16), π_{ij} can be calculated by

$$\pi_{ij} = \frac{\eta_{ij}}{\sum_{h=1}^{K} \eta_{ih}} \tag{30}$$

In addition, we incorporate the weighted mean template into (30) then obtain

$$\pi_{ij} = \frac{\prod_{q \in \Lambda_i} (\eta_{ij})^{\frac{w_q}{R_i}}}{\prod_{q \in \Lambda_i} (\sum_{h=1}^{K} \eta_{ih})^{\frac{w_q}{R_i}}} \tag{31}$$

Similarity, with constrained multiplier β_{ij}, we compute the derivative of k_{ijm} as

$$\frac{\partial}{\partial k_{ijm}} \left[J(\Theta) - \sum_{i=1}^{N} \beta_{ij} \left(\sum_{m=1}^{M} k_{ijm} - 1 \right) \right] = 0 \tag{32}$$

Under the constrains (19), k_{ijm} is compute by

$$k_{ijm} = \frac{\eta_{ij} + z_{ijm}}{\sum_{h=1}^{K} \eta_{ij} \sum_{n=1}^{M} z_{ihn}} \tag{33}$$

The adaptive structure tensor based weight mean template is also incorporated into (33), and then we have:

$$k_{ijm} = \frac{\prod_{q \in \partial_i} (\eta_{ij} z_{ijk})^{\frac{w_q}{R_i}}}{\prod_{q \in \Lambda_i} (\sum_{h=1}^{K} \eta_{ih} \sum_{n=1}^{M} z_{ihn})^{\frac{w_q}{R_i}}} \tag{34}$$

To make the objective function (22) more detailed, we use (18) in (22) to get the Equation (35). Following [15], we obtain

$$\begin{aligned} J(\Phi) &= \sum_{i=1}^{N} \sum_{j=1}^{K} \eta_{ij} \left\{ \log \pi_{ij} + \sum_{m=1}^{M} z_{ijm} \times \log k_{ijm} + E_\Phi \right. \\ &\quad \left. \left(\sum_{q \in \Lambda_i} \frac{w_q}{R_i} \log S(y_i \mid \theta_{jm}) \right) \right] \Bigg\} \\ &= \sum_{i=1}^{N} \sum_{j=1}^{K} \eta_{ij} \left\{ \log \pi_{ij} + \sum_{m=1}^{M} z_{ijm} \right. \\ &\quad \left\{ \log k_{ijM} + \frac{\tau_{jm}}{2} \log \frac{\tau_{jm}}{2} - \frac{1}{2} \log(2\pi) \right. \\ &\quad - \log \Gamma(\frac{\tau_{jm}}{2}) - \frac{1}{2} \log |\Sigma| + \sum_{q \in \Lambda_i} \frac{w_q}{R_i} \\ &\quad \left[\frac{L + \tau_{jm}}{2} E_\Phi(\log u_{ijm}) - \frac{\tau_{jm}}{2} u_{ijm} \right. \\ &\quad \left. \left. - \frac{1}{2} u_{ijm} (y_i - \mu_{jm})^T \Sigma_{jm}^{-1} (y_i - \mu_{jm}) \right] \right\} \Bigg\} \end{aligned} \tag{35}$$

$$E_\Phi(\log u_{ijm}) = \log u_{ijm} - \log(\frac{\tau_{jm} + L}{2}) + \psi(\frac{\tau_{jm} + L}{2}) \tag{36}$$

Parameters $(\mu_{jm}, \Sigma_{jm}, \tau_{jm})$ are estimated through solving Eq.(35) which can be modified by omitting some constant entries shown in Eq. (37) - (39) respectively. The derivatives of parameters μ_{jm} and Σ_{jm} can be gained through Eq.(37) and Eq. (38), and their update are calculated as follows:

$$\begin{aligned} J_{\mu jm} = \sum_{i=1}^{N} \sum_{j=1}^{K} \eta_{ij} \sum_{m=1}^{M} z_{ijk} \left[\sum_{q \in \Lambda_i} \frac{w_q}{R_i} (\frac{L + \tau_{jm}}{2}) E_\Phi(\log u_{ijm}) \right. \\ \left. - \frac{\tau_{jm}}{2} u_{ijm} - \frac{\tau_{jm}}{2} u_{ijm} (y_i - \mu_{jm})^T \Sigma_{jm}^{-1} (y_i - \mu_{jm}) \right] \end{aligned} \tag{37}$$

$$\begin{aligned} J_{\Sigma_{jm}^{-1}} = J_{\mu_{jk}} = \sum_{i=1}^{N} \sum_{j=1}^{K} \eta_{ij} \sum_{m=1}^{M} z_{ijk} \left[-\frac{1}{2} \log |\Sigma| \sum_{q \in \Lambda_i} \frac{w_q}{R_i} (\frac{L + \tau_{jm}}{2}) \right. \\ \left. E_\Phi(\log u_{ijm}) - \frac{\tau_{jm}}{2} u_{ijm} - - \frac{1}{2} u_{ijk} (y_i - \mu_{jm})^T \Sigma_{jk}^{-1} (y_i - \mu_{jk}) \right] \end{aligned} \tag{38}$$

$$J_{vjk}=\sum_{i=1}^{N}\sum_{j=1}^{K}\eta_{ij}\left\{\sum_{m=1}^{M}z_{ijm}\{\frac{\tau_{jm}}{2}\log\frac{\tau_{jm}}{2}-\log\Gamma(\frac{\tau_{jm}}{2})+\sum_{q\in\Lambda_i}\frac{w_q}{R_i}\left[\frac{L+\tau_{jm}}{2}E_{\Phi}(\log u_{ijm})-\frac{\tau_{jm}}{2}u_{ijm}-\frac{1}{2}u_{ijm}(y_i-\mu_{jm})^T\Sigma_{jm}^{-1}(y_i-\mu_{jm})\right]\right\}\right\} \quad (39)$$

$$\mu_{jm}^{(t+1)}=\frac{\sum_{i=1}^{N}\eta_{ij}^{(t)}\sum_{q\in\Lambda_i}\frac{w_q}{R_i}z_{ijm}^{(t)}u_{ijm}^{(t)}y_i}{\sum_{i=1}^{N}\eta_{ij}^{(t)}z_{ijm}^{(t)}u_{ijm}^{(t)}} \quad (40)$$

At last, the derivative of J_{vjk} with respect to v_{jk} is set to be zero and we have

$$\Sigma_{jm}^{(t+1)}=\frac{\sum_{i=1}^{N}\eta_{ij}^{(t)}\sum_{q\in\Lambda_i}\frac{w_q}{R_i}z_{ijm}^{(t)}u_{ijm}^{(t)}(y_i-\mu_{jm})^T\Sigma_{jm}^{-1}(y_i-\mu_{jm})}{\sum_{i=1}^{N}\eta_{ij}^{(t)}z_{ijm}^{(t)}} \quad (41)$$

$$\log\left(\frac{\tau_{jm}^{(t+1)}}{2}\right)-\psi\left(\frac{\tau_{jm}^{(t+1)}}{2}\right)+1+\frac{\sum_{i=1}^{N}\eta_{ij}z_{ijm}\sum_{q\in\Lambda_i}\frac{w_q}{R_i}(\log u_{ijm}-u_{ijm})}{\sum_{i=1}^{N}\eta_{ij}z_{ijm}}+\psi\left(\frac{\tau_{jm}^{(t+1)}+L}{2}\right)-\log\left(\frac{\tau_{jm}^{(t)}+L}{2}\right)=0 \quad (42)$$

For clarity, we summarize the proposed method as follows:

(1) Initialize the parameter set $\Phi=\{\pi_{ij},k_{ijm},\mu_{jm},\Sigma_{jm},\tau_{jm}\}$.

(2) E-step:

- Use equation (25) to compute the posterior probability η_{ij};
- Use equation (26) to compute the sub-posterior probability z_{ijm};
- Use equation (27) to compute the factor μ_{ijm}.

(3) M-step: update the parameter set Φ.

- Use equation (31) to update the prior probability π_{ij};
- Use equation (34) to update the sub-prior probability k_{ijm};
- Use equations (40), (41), (42) to update the quantities $\mu_{jm},\Sigma_{jm},\tau_{jm}$, respectively.

(4) Repeat steps 2 to 4 until the objective function converges.

6 Experimental Results

In experiments, in addition to the synthetic SAR image set, our proposed HSMM based segmentation was also evaluated on general-used real SAR image sets including SAR Sea-Ice Image set, RADARSAT-1 SAR image set and Pauli RGB Image set. Three representative FMM based image segmentation approaches such as MSMM [25], SVFMM [40] and HMRF [41] were compared with our method. The above-mentioned for methods were implemented in a platform with Intel 2.2 GHZ CPU, Corsair 2 GB RAM, and MATLAB 2009b software. we set the number of classes K to 8, the paramters $\Phi=\{\pi_{ij},k_{ijm},\mu_{jm},\Sigma_{jm},\tau_{jm}\}$ was initialized by K-means algorithms.

6.1 Synthetic Images

This experiment evaluates the four aforementioned FMM based approaches on a synthetic SAR image with size of 512×512, which in fact composes of four classes. Figure 1(a) shows the original clean SAR image. Figure 1(b) is generated by adding speckle noise into the Figure 1(a). Its peak-signal-to-noise-ratio is 5.15 dB. In addition, the overall accuracy ratio (OAR) index was employed for quantitative comparison of segmentation performance, which is the ratio of the number corrected segmented pixels to the number of whole image pixels, defined by

$$OAR=\frac{\text{number of corrected segmented pixels}}{\text{number of whole image pixels}}\times100\% \quad (43)$$

Higher OAR value, better performance of the SAR image segmentation approach. Obviously, the range of OAR value is from 0 to 100.

In this experiment, we used the traditional k-means clustering technique to initialize the four segmentation algorithms. Figure 1(c) to Figure 1(f) display the experimental results of HMRF, MSMM, SVFMM and our proposed HSMM, respectively. We can see from Figure 1 that the four approaches can generate relatively good segmentation results on the whole. However, carefully observing the results, one can find out that HMRF and SVFMN fail to overcome the influence of speckle noise. Both of the regions framed in red and yellow show the drawbacks of the two methods. From Figure 1(c) to Figure 1(f), we can see that compared with other three FMM based clustering method, the HSMM gives rise to the most accurate partition image and is robust to speckle noise. It should be addressed that the time consumption of our method is also satisfying, with 36.45s. Although this speed is higher than that of MSMM's, the OAR value of our segmentation result can obtain 95.35%. Better performance comes at a cost.

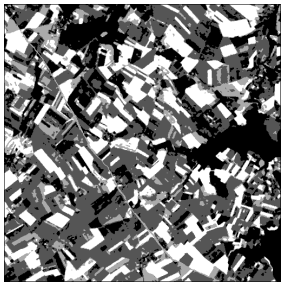

(a) Original synthetic SAR image

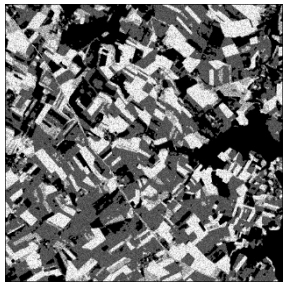

(b) SAR image with speckle noise, PSNR = 5.15 dB

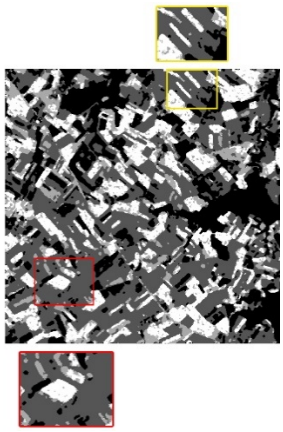

(c) HMRF, OAR = 87.52%

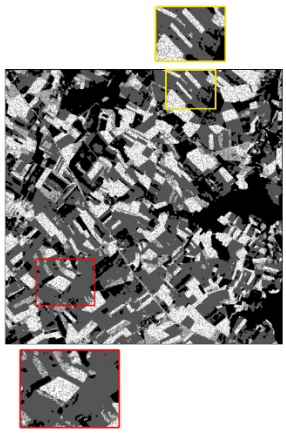

(d) SVFMM, OAR = 89.48%

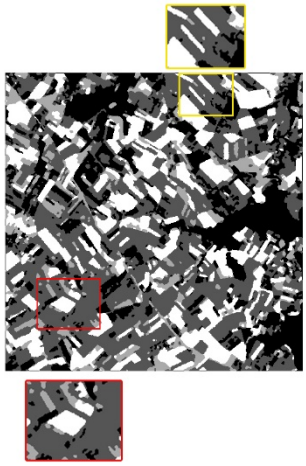

(e) MSMM, OAR = 92.18%

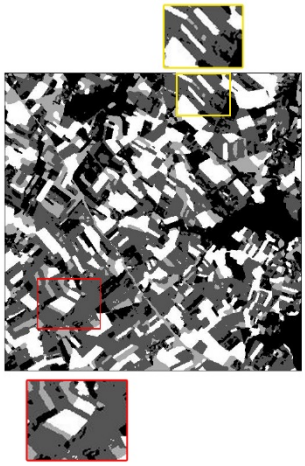

(f) HSMM, OAR = 94.29%

Figure 1. Comparison of image segmentation on synthetic image

6.2 Synthetic Images

In this experiment, a real SAR image of the Gulf of St. Lawrence on 20th Feb, in 1998, was employed to evaluate the segmentation performance of the our methods in accuracy and robustness, which was captured by the RADARSAT ScanSAR, a SAR working at C-Band with pixel spacing of 100 m. The SAR Image contains four clusters: land cluster, water cluster, gray ice cluster and gray-white ice cluster. The land appears at the bottom of image in white; water centers around the land region in dark; gray ice the image almost occupies the top half of the image; gray-white ice appears the rest of the SAR image. See Figure 2(a) for details.

The reason for selecting this SAR image lies in the observation there are many narrow belts in the gray ice area which is proper to assess the capability of segmentation algorithm in terms of accuracy. Figure 2(b) displays the ground truth of the sea-ice SAR image segmentation, which was labeled manually by specialty researcher. The image segmentation results

by the four methods, i.e., SVFMM, HMRF, MSMM and HSMM, are illustrated in Figure 2(c) to Figure 2(f), respectively. From the results shown in Figure 2(c), we can clearly see that the result yielded by SVFMM contains much noise. The SVFMM based segmentation method performs poor for SAR image. Its OAR value is 80.92%. By contrast, HMRF and MSMM show good performance in segmentation accuracy, shown in Figure 2(d) and Figure 2(e). They can gain high OAR values. The OAR values of HMRF and MSMM is 83.88% and 91.29%, respectively. However, HMRF is time consuming. Figure 2(f) shows the performance of our proposed HSMM. Again, we observe that the HSMM gains the best segmentation results. Although its computation time is slight higher than HSMM, its OAR value is the highest.

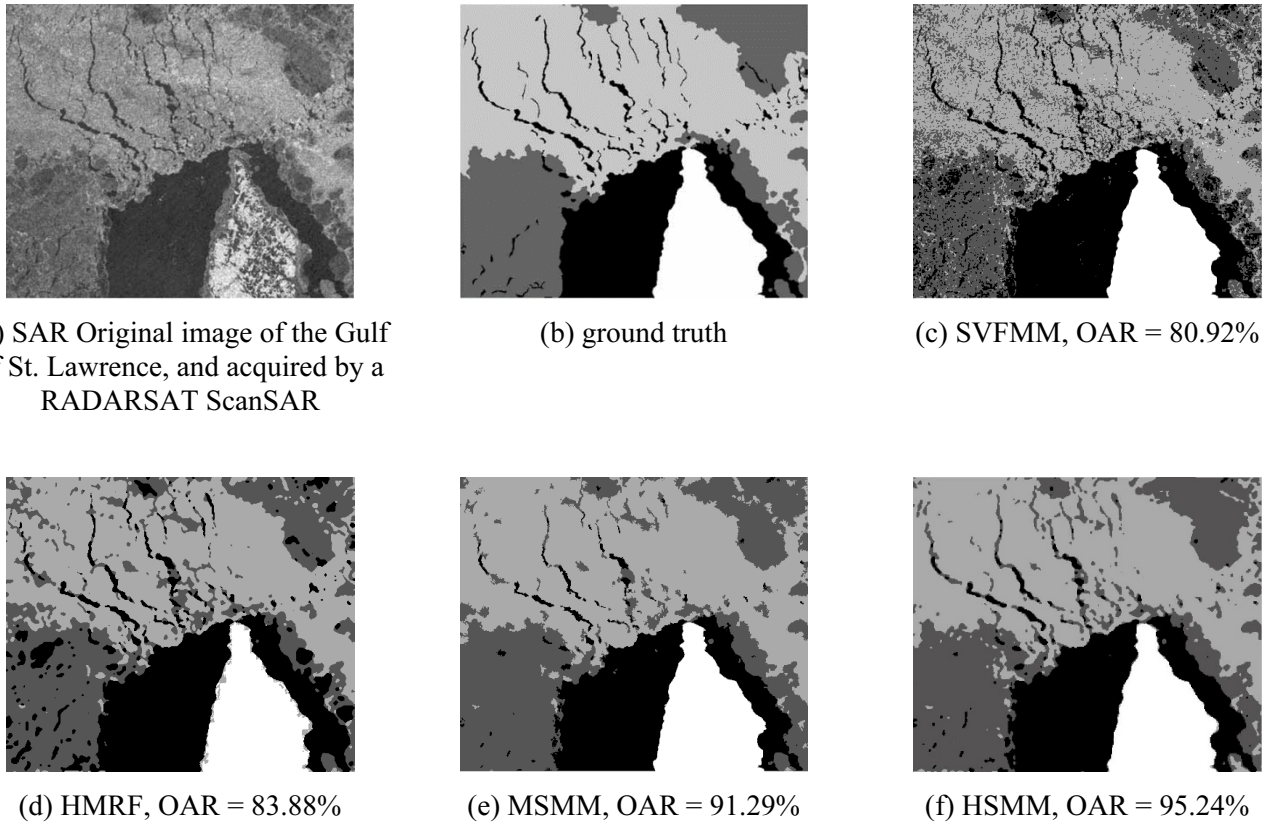

(a) SAR Original image of the Gulf of St. Lawrence, and acquired by a RADARSAT ScanSAR

(b) ground truth

(c) SVFMM, OAR = 80.92%

(d) HMRF, OAR = 83.88%

(e) MSMM, OAR = 91.29%

(f) HSMM, OAR = 95.24%

Figure 2. Comparison of image segmentation on the sea-ice SAR image

6.3 RADARSAT-1 Image

In this experiment, we assessed the quality of segmentation results by different methods on the RADARSAT-1 SAR image. Researched and developed by Canada, RADARSAT-1 is a complicated Earth observation and radar satellite that can detect environmental changes and natural resources of our planet. The original SAR image of RADARSAT-1 (Figure 3(a)) shows one part of Northwest Territories (NWT) in Canada, which is the second largest territory in Canada with an area of ~ 1.17×10^6 km^2. The upper part of the image shows Franklin Mountain, while the lower part shows Mackenzie Mountain. Both mountains are separated by Mackenzie River, which is the dark region in the middle of the image. The river is 1800 kilometers long and 1.6 kilometers wide on average (in some places, it is 6 kilometers wide). It is 8-9 meters deep and covers a drainage area of ~ 1.8×10^6 km^2.

We set the number of classes to 3. Figire 3(b) to Figire 3(e) show the results of different methods. The SVFMM obviously yields bad segmentation while the other methods seem to segment the image clearly. From Figure 3(c) to Figire 3(d), the HMRF tends to over-segment (for better or for worse), and is quite computationally intensive; the MSMM exhibits better segmentation, but it omits some regions of the mountains (from the bottom left in Figure 3(d)). From Figure 3(e), the HSMM can segment the image better than the MSMM, some details are clearer, and the computation time is the shortest across all methods.

6.4 Pauli RGB Image

Finally, to assess the segmentation quality of HSMM on the polarimetric synthetic aperture radar (POLSAR) image, we extracted the red-green-blue (RGB) composite of Pauli decomposition from polarimetric L-band data, NASA/JPL AIRSAR in Flevoland, Netherlands (http://earth.eo.esa.int/polsarpro/

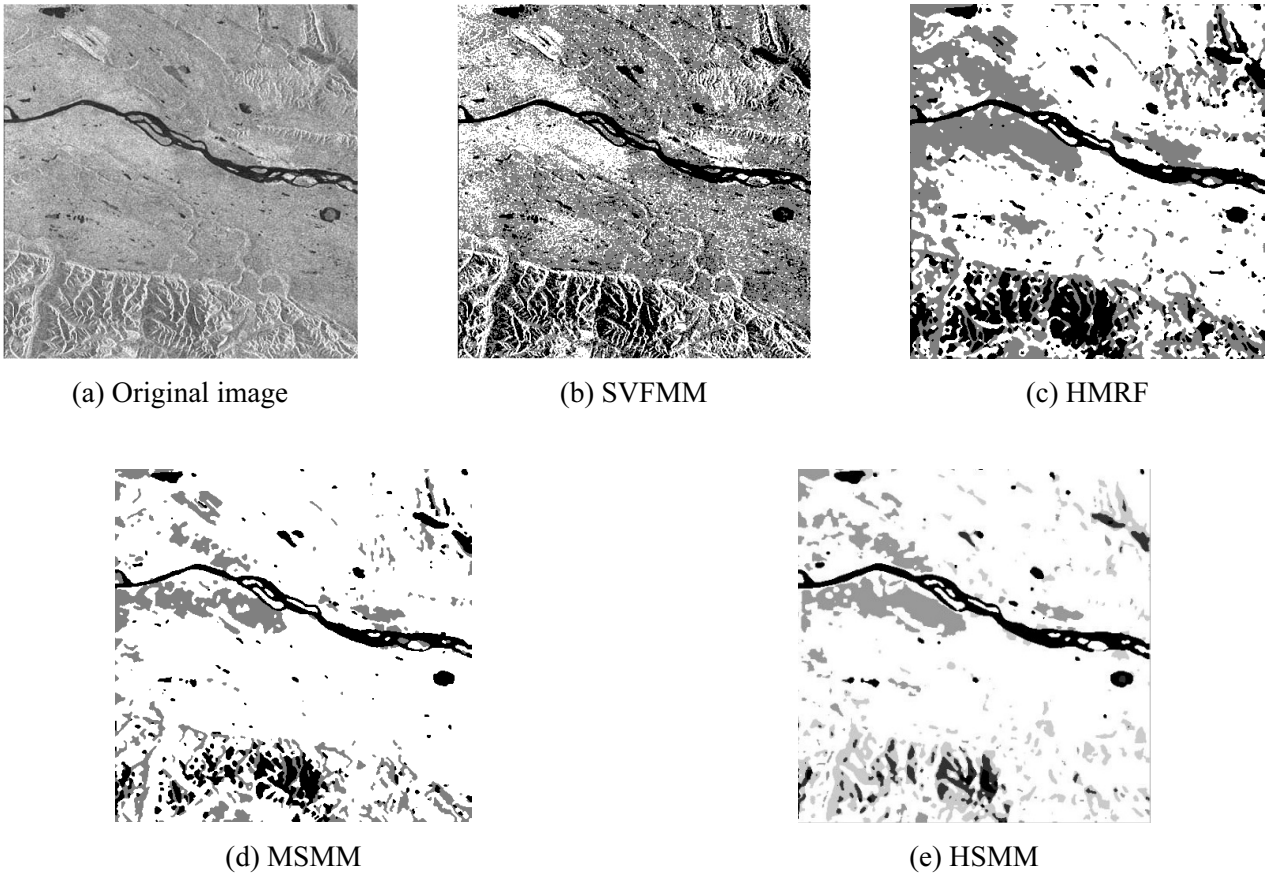

(a) Original image (b) SVFMM (c) HMRF

(d) MSMM (e) HSMM

Figure 3. Segmentation of a RADARSAT-1 SAR image that represents a portion of the Northwest Territories (NWT) in Canada

datasets.html.). Yu et al. utilized the sub-image and mask [45]. We adopted the same Pauli RGB image (282×383) as well as the real image of the Earth's surface (Figure 4(a) to Figure 4(b)).

To compare segmentation performance of the different methods, every generic label is required to be closely connected with a ground-truth class, which is color-coded. We completed the connection by finding a mapping of generic labels, which helped to maximize the OAR and is defined in equation (40). The mapping is completed by trying every possible mapping of generic labels with ground-truth labels and selecting the most accurate label. It is worth noting that there are no labels for pixels of the Pauli RGB image provided by the ground-truth in Figure 4(b). As a result, OAR can be calculated when the truth offers a label. Figure 4(c) to Figure 4(e) show the segmentation results for the HMRF, MSMM, and HSMM, respectively. We can conclude that that: (1) the HMRF yields bad segmentation, with some noise; (2) the MSMM and HSMM both exhibit better performances. However, when comparing Figure 4(d) with Figure 4(e), we find that the MSMM misclassifies one box in the center of the image, i.e. the blue-color box, even though better segmentation is obtained on the image's margin. Nevertheless, a visual inspection suggests that the HSMM is much preferable than the MSMM.

In addition, we compared the computation time of the different methods, and these times are shown in Table 1. From Table 1 we can clearly see that our proposed HSMM method is faster than both the SVFMM and HMRF, and acceptably slower than the MSMM.

7 Conclusions

This work introduced a segmentation method for SAR image using the herein proposed HSMM, which can improve the performance of FMM based image segmentation on robustness to speckle noise. The proposed HSMM can accurately represent image class with anisotropic distribution. This is mainly contributed to the incorporated mean template, which employs a non-linear structure tensor to enhance its adaptability to image contents. The HSMM based image segmentation model was solved by the EM algorithm and experimental results show that our HSMM is more robust compared to the existing popular FMM based SAR image segmentation approaches.

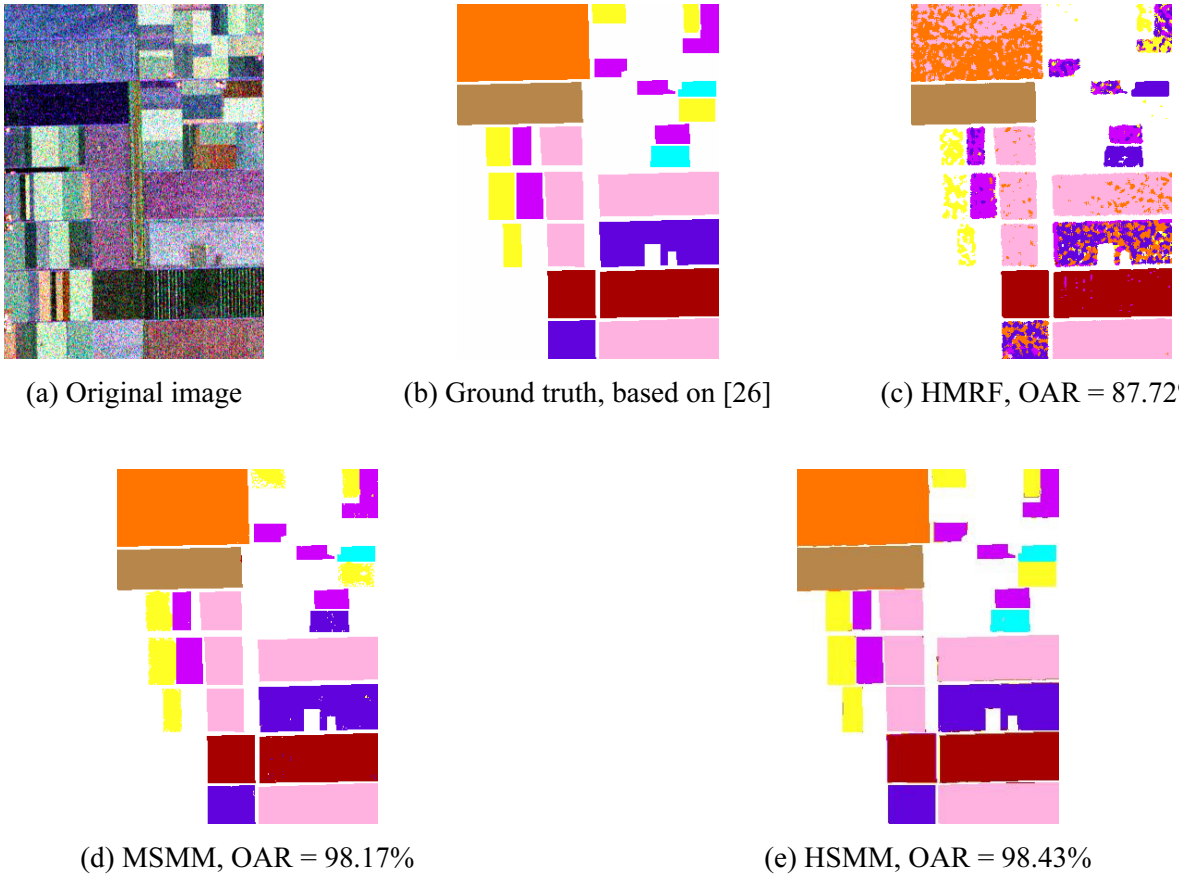

(a) Original image (b) Ground truth, based on [26] (c) HMRF, OAR = 87.72%

(d) MSMM, OAR = 98.17% (e) HSMM, OAR = 98.43%

Figure 4. Segmentation of a Pauli RGB image (282×383 pixels) extracted from the polarimetric L-band data, NASA/JPL AIRSAR of Flevoland, Netherlands

Table 1. Computation time of different methods, on various types of SAR images (s)

Image/Methods	SVFMM	HMRF	MSMM	HSMM
Synthetic SAR image	153.87	566.1	22.38	47.23
Sea-Ice SAR image	40.34	534.74	16.65	29.38
RADARSAT-1 image	25.44	245.81	9.58	12.34
Pauli RGB image	-	711.86	48.63	72.88

In addition to I IoT satellite system, our method can be also used to space exploration. Space exploration is a necessary way for human beings to grope after the universe and seek long-term development. Carrying out space exploration of lunar and farther stars has become one of important human space activities, recently. As an extremely important exploration tool, space detectors are developing rapidly towards the aspects of intelligentization, multi-loads and long-life. In space exploring process, the space detectors often carry limited energy. For making full use of energy and efficient realization of its application, an alternative way is to intelligently coordinate and control the various imaging loads in space detectors for observing and monitoring planets. Specifically, it is non-essential for the detectors to boot up imaging instruments at the same time. Observation imagery from a certain imaging instrument could well be analyzed and identified by central control systemin detector to select and boot up an appropriate imaging-load for long-term object-of-interest observation and monitoring. SAR is a proper candidate, due to its capability of acquisition under complicated conditions. The proposed method can be applied to online intelligent perception of SAR satellite to control various imaging instruments of space detector for efficiently improving energy usage.

References

[1] L. Sun, C. Ma, Y. Chen, Y. Zheng, H. Shim, Z. Wu, B. Jeon, Low Rank Component Induced Spatial-spectral Kernel Method for Hyperspectral Image Classification, *IEEE Transactions on Circuits and Systems for Video Technology*, 2020. DOI: 10.1109/TCSVT.2019.2946723.

[2] J. Han, D. Zhang, G. Cheng, L. Guo, J. Ren, Object Detection in Optical Remote Sensing Images Based on Weakly Supervised Learning and High-level Feature Learning, *IEEE Transactions on Geoscience and Remote Sensing*, Vol. 53, No. 6, pp. 3325-3337, June, 2015.

[3] M. Wang, Y. Gao, K. Lu, Y. Rui, View-Based Discriminative Probabilistic Modeling for 3D Object Retrieval and Recognition, *IEEE Transactions on Image Processing*, Vol. 22, No. 4, pp. 1395-1407, April, 2013.

[4] X. Xing, D. Wen, H. Chang, L. Chen, Z. Yuan, Highway Deformation Monitoring Based on an Integrated CRInSAR Algorithm - Simulation and Real Data Validation, *International Journal of Pattern Recognition and Artificial Intelligence*, Vol. 32, No. 11, pp. 1-19, November, 2018

[5] D. Zhang, D. Meng, J. Han, Co-saliency Detection via a Self-paced Multiple-instance Learning Framework, *IEEE Transactions on Pattern Analysis and Machine Intelligence*, Vol. 39, No. 5, pp. 865-878, May, 2017.

[6] J. Han, K. Ngan, M. Li, H. Zhang, Unsupervised Extraction of Visual Attention Objects in Color Images, *IEEE Transactions on Circuits and Systems for Video Technology*, Vol. 16, No. 1, pp. 141-145, January, 2006.

[7] Y. Zheng, X. Wang, G. Zhang, B. Xiao, F. Xiao, J. Zhang, Multi-Kernel Coupled Projections for Domain Adaptive Dictionary Learning, *IEEE Transactions on Multimedia*, Vol. 21, No. 9, pp. 2292-2304, September, 2019.

[7] S. Luo, L. Tong, Y. Chen, A Multi-region Segmentation Method for SAR Images Based on the Multi-texture model, *IEEE Transactions on Image Processing*, Vol. 27, No. 5, pp. 2560-2574, May, 2018.

[9] Q. Yu, D. A. Clausi, Filament Preserving Model (FPM) Segmentation Applied to SAR Sea-Ice Imagery, *IEEE Transactions on Geoscience and Remote Sensing*, Vol. 44, No. 12, pp. 3687-3694, December, 2006.

[10] R. Fjortoft, Y. Delignon, W. Pieczynski, M. Sigelle, F. Tupin, Unsupervised Classification of Radar Images Using Hidden Markov Chains and Hidden Markov Random Fields, *IEEE Transactions on Geoscience and Remote Sensing*, Vol. 41, No. 3, pp. 675-686, March, 2003.

[11] C. Carson, S. Belongie, H. Greenspan, J. Malik, Blobworld: Image Segmentation Using Expectation-maximization and Its Application to Image Querying, *IEEE Transactions on Pattern Analysis and Machine Intelligence*, Vol. 24, No. 8, pp. 1026-1038, August, 2002.

[12] H. Permuter, J. Francos, I. Jermyn, A Study of Gaussian Mixture Models of Color and Texture Features for Image Classification and Segmentation, *Pattern Recognition*, Vol. 39, No. 4, pp. 695-706, April, 2006.

[13] G. Xia, G. Liu, W. Yang, Meaningful Objects Segmentation from SAR Images via a Multiscale Nonlocal Active Contour Model, *IEEE Transactions on Geoscience and Remote Sensing*, Vol. 54, No. 3, pp. 1860-1873, March, 2016.

[14] U. Javed, M. M. Riaz, A. Ghafoor, T. A. Cheema, SAR Image Segmentation Based on Active Contours with Fuzzy Logic, *IEEE Transactions of Aerospace and Electronic Systems*, Vol. 52, No. 1, pp. 181-188, February, 2016.

[15] C. Liu, J. Yang, J. Yin, W. An, Coastline Detection in SAR Images Using a Hierarchical Level Set Segmentation, *IEEE Journal of Selected Topics in Applied Earth Observations and Remote Sensing*, Vol. 9, No. 11, pp. 4908-4920, November, 2016.

[16] D. Xiang, Y. Ban, W. Wang, Y. Su, Adaptive Superpixel Generation for Polarimetric SAR Images with Local Iterative Clustering and SIRV Model, *IEEE Transactions on Geoscience and Remote Sensing*, Vol. 55, No. 6, pp. 3115-3131, June, 2017.

[17] W. Wang, D. Xiang, Y. Ban, J. Zhang, J. Wan, Superpixel Segmentation of Polarimetric SAR Images Based on Integrated Distance Measure and Entropy Rate Method, *IEEE Journal of Selected Topics in Applied Earth Observations and Remote Sensing*, Vol. 10, No. 9, pp. 4045-4058, September, 2017.

[18] F. Qin, J. Guo, F. Lang, Superpixel Segmentation for Polarimetric SAR Imagery Using Local Iterative Clustering, *IEEE Geoscience and Remote Sensing Letters*, Vol. 12, No. 1, pp. 13-17, January, 2015.

[19] Y. Duan, F. Liu, L. Jiao, Sketching Model and Higher Order Neighborhood Markov Random Field-based SAR Image Segmentation, *IEEE Geoscience and Remote Sensing Letters*, Vol. 13, No. 11, pp. 1686-1690, November, 2016.

[20] F. Wang, Y. Wu, M. Li, P. Zhang, Q. Zhang, Adaptive Hybrid Conditional Random Field Model for SAR Image Segmentation, *IEEE Transactions on Geoscience and Remote Sensing*, Vol. 55, No. 1, pp. 537-550, January, 2017.

[21] F. Wang, Y. Wu, P. Zhang, M. Li, Unsupervised SAR Image Segmentation Using Ambiguity Label Information Fusion in Triplet Markov Fields Model, *IEEE Geoscience and Remote Sensing Letters*, Vol. 14, No. 9, pp. 1479-1483, September, 2017.

[22] L. Wan, T. Zhang, Y. Xiang, H. You, A Robust Fuzzy C-means Algorithm Based on Bayesian Nonlocal Spatial Information for SAR Image Segmentation, *IEEE Journal of Selected Topics in Applied Earth Observations and Remote Sensing*, Vol. 11, No. 3, pp. 896-906, March, 2018.

[23] R. Shang, P. Tian, L. Jiao, B. Hou, X. Zhang, A Spatial Fuzzy Clustering Algorithm with Kernel Metric Based on Immune Clone for SAR Image Segmentation, *IEEE Journal of Selected Topics in Applied Earth Observations and Remote Sensing*, Vol. 9, No. 4, pp. 1640-1652, April, 2016.

[24] Y. Zheng, X. Zhou, B. Jeon, J. Shen, H. Zhang, Multi-Scale Patch Prior Learning for Image Denoising Using Student's- t Mixture Model, *Journal of Internet Technology*, Vol. 18, No. 7, pp. 1553-1560, December, 2017.

[25] H. Zhang, Q. M. J. Wu, T. M. Nguyen, X. Sun, Synthetic Aperture Radar Image Segmentation by Modified Student's t-mixture Model, *IEEE Transactions on Geoscience and Remote Sensing*, Vol. 52, No. 7, pp. 4391-4403, July, 2014.

[26] Y. Chen, J. Li, H. Zhang, Y. Zheng, B. Jeon, Q. M. J. Wu, Non-local-based Spatially Constrained Hierarchical Fuzzy C-means Method for Brain Magnetic Resonance Imaging Segmentation, *IET Image Processing*, Vol. 10, No. 11, pp. 865-876, November, 2016.

[27] C. Xu, L. Xu, Z. Gao, S. Zhao, H. Zhang, Y. Zhang, X. Du, S. Zhao, D. Ghista, Direct Delineation of Myocardial Infarction without Contrast Agents Using a Joint Motion Feature Learning Architecture, *Medical Image Analysis*, Vol. 50, pp. 82-94, December, 2018.

[28] Y. Zheng, B. Jeon, L. Sun, J. Zhang, H. Zhang, Student's t-Hidden Markov Model for Unsupervised Learning Using Localized Feature Selection, *IEEE Transactions on Circuits and Systems for Video Technology*, Vol. 28, No. 10, pp. 2586-2598, October, 2018.

[29] A. Thangarajah, Q. M. J. Wu, Y. Yang, Fusion-based Foreground Enhancement for Background Subtraction Using Multivariate Multi-model Gaussian Distribution, *Information Science*, No. 430, pp. 414-431, March, 2018.

[30] T. M. Nguyen, Q. M. J. Wu, Robust Student's- t Mixture Model with Spatial Constraints and Its Application in Medical Image Segmentation, *IEEE Transactions on Medical Imaging*, Vol. 31, No. 1, pp. 103-116, January, 2012.

[31] J. Zhang, Q. Yu, Y. Zheng, H. Zhang, J. Wu, Regularization Parameter Selection for TV Image Denoising Using Spatially Adaptive Local Spectral Response, *Journal of Internet Technology*, Vol. 17, No. 6, pp. 1117-1124, November, 2016.

[32] H. Zhang, Q. M. J. Wu, T. M. Nguyen, A Robust Fuzzy Algorithm Based on Student's t-distribution and Mean Template for Image Segmentation Application, *IEEE Signal Processing Letters*, Vol. 20, No. 2, pp. 117-120, February, 2013.

[33] F. Xu, W. Cao, Dynamic Axial Crashing of Tailor-welded Blanks (TWBs) Thin-walled Structures with Top-hat Shaped Section, *Advances in Engineering Software*, Vol. 96, pp. 70-82, 2016.

[34] S. Sanjay-Gopal, T. J. Hebert, Bayesian Pixel Classification Using Spatially Variant Finite Mixtures and the Generalized EM Algorithm, *IEEE Transactions on Image Processing*, Vol. 7, No. 7, pp. 1014-1028, July, 1998.

[35] Y. Zhang, M. Brady, S. Smith, Segmentation of Brain MR Images through a Hidden Markov Random Field Model and the Expectation-maximization Algorithm, *IEEE Transactions on Medical Imaging*, Vol. 20, No. 1, pp. 45-57, January, 2001.

[36] J. I. Michael, A. Robert, Hierarchical Mixtures of Experts and the EM Algorithm, *Neural Computation*, Vol. 6, No. 2, pp. 181-214, March, 1994.

[37] S. P. Chatzis, D. I. Kosmopoulos, T. A. Varvarigou, Robust Sequential Data Modeling Using an Outlier Tolerant Hidden Markov Model, *IEEE Transactions on Pattern Analysis and Machine Intelligence*, Vol. 31, No. 9, pp. 1657-1669, September, 2009.

[38] Z. Gao, Y. Li, Y. Sun, J. Yang, H. Xiong, H. Zhang, X. Liu, W. Wu, D. Liang, S. Li, Motion Tracking of the Carotid Artery Wall from Ultrasound Image Sequences: A Nonlinear State-space Approach, *IEEE Transactions on Medical Imaging*, Vol. 37, No. 1, pp. 273-283, January, 2017.

[39] H. Zhang, Q. M. J. Wu, T. M. Nguyen, Incorporating Mean Template into Finite Mixture Model for Image Segmentation, *IEEE Transactions on Neural Networks and Learning Systems*, Vol. 24, No. 2, pp. 328-335, February 2013.

[40] K. Blekas, A. Likas, N. P. Galatsanos, I. E. Lagaris, A Spatially Constrained Mixture Model for Image Segmentation, *IEEE Transactions on Neural Networks*, Vol. 16, No. 2, pp. 494-498, March, 2005.

[41] S. P. Chatzis, T. A. Varvarigou, A Fuzzy Clustering Approach toward Hidden Markov Random Field Models for Enhanced Spatially Constrained Image Segmentation, *IEEE Transactions on Fuzzy Systems*, Vol. 16, No. 5, pp. 1351-1361, October, 2008.

[42] L. Kong, H. Zhang, Y. Zheng, Y. Chen, J. Zhu, Q. M. J. Wu, Image Segmentation Using a Hierarchical Student's- t mixture Model, *IET Image Processing*, Vol. 11, No. 11, pp. 1094 -1102, November, 2017.

[43] V. Estellers, S. Soatto, X. Bresson, Adaptive Regularization with the Structure Tensor, *IEEE Transactions on Image Processing*, Vol. 24, No. 6, pp. 1777-1790, June, 2015.

[44] Y. Zheng, J. Beon, W. Zhang, Y. Chen, Adaptively Determining Regularization Parameters in Nonlocal Total Variation Regularization for Image Denoising, *Electronics Letters*, Vol. 51, No. 2, pp. 144-145, January, 2015.

[45] P. Yu, A. K. Qin, D. A. Clausi, Unsupervised Polarimetric SAR Image Segmentation and Classification Using Region Growing with Edge Penalty, *IEEE Transactions on Geoscience and Remote Sensing*, Vol. 50, No. 4, pp. 1302-1317, April, 2012.

Biographies

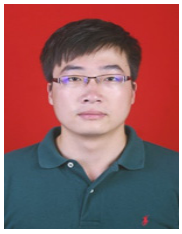

Huilin Ge received his M.S. degree in Control Theory and Control Engineering from Jiangsu University of Science and Technology, Jiangsu, China, in 2013. He is now a Ph.D. student of Naval & Ocean Engineering in Jiangsu University of Science and Technology. His research interest is image processing and anaylysis.

Yahui Sun received the B.S. degree in Software Engineering from Binjiang College, Nanjing University of Information Science and Technology in 2018. She is pursuing M.S. degree at the School of Computer and Software in Nanjing University of Information Science and Technology. Her research interest is image processing.

Yueh-Min Huang received his M.S. and Ph.D. degrees in Electrical Engineering from the University of Arizona in 1988 and 1991 respectively. He is a Chair Professor in Department of Engineering Science and Institute of Education, National Cheng-Kung University, Taiwan. His research interests include e-Learning, multimedia communications, and artificial intelligence.

Se-Jung Lim received her M.S. and Ph.D. degrees from Chonnam National University in 2010 and in 2016. She is currently an assistant professor of Liberal Arts & Convergence Studies Division of Convergence at Honam University. Her research interests include wireless wensor Networks, Iots and Big Data.